

Effect of Mesostructured Layer upon Crystalline Properties and Device Performance on Perovskite Solar Cells

Andrea Listorti,^{*,†,‡,○} Emilio J. Juarez-Perez,^{§,○} Carlos Frontera,^{||} Vittoria Roiati,^{†,⊥}
Laura Garcia-Andrade,^{§,¶} Silvia Colella,^{‡,▽} Aurora Rizzo,[‡] Pablo Ortiz,[¶] and Ivan Mora-Sero^{*,§}

[†]Center for Bio-Molecular Nanotechnology, Fondazione Istituto Italiano di Tecnologia, Via Barsanti, 73010 Arnesano, Lecce, Italy

[‡]Istituto di nanotecnologia CNR Nanotec, Via Arnesano 16, 73100 Lecce, Italy

[§]Photovoltaic and Optoelectronic Devices Group, Departament de Física, Universitat Jaume I, 12071 Castelló, Spain

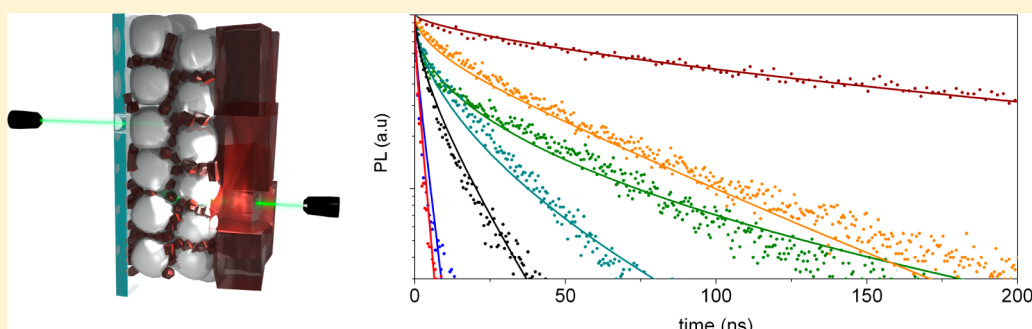
^{||}Institut de Ciència de Materials de Barcelona, ICMAB-CSIC, Campus de la UAB, Cerdanyola del Vallès, Barcelona 08193, Spain

[⊥]Dept. of Physics, Politecnico di Milano, Piazza Leonardo da Vinci 32, 20133 Milano, Italy

[¶]Grupo de Diseño de Productos y Procesos, Departamento de Ingeniería Química, Universidad de los Andes, Cr 1 aEste 19A-40, 110111 Bogotá, Colombia

[▽]Dipartimento di Matematica e Fisica “E. de Giorgi”, Università del Salento, Via Arnesano 16, 73100, Lecce Italy

Supporting Information



ABSTRACT: One of the most fascinating characteristics of perovskite solar cells (PSCs) is the retrieved obtainment of outstanding photovoltaic (PV) performances notwithstanding important device configuration variations. Here we have analyzed $\text{CH}_3\text{NH}_3\text{PbI}_{3-x}\text{Cl}_x$ in planar or in mesostructured (MS) configurations, employing both titania and alumina scaffolds, fully infiltrated with perovskite material or presenting an overstanding layer. The use of the MS scaffold induces to the perovskite different structural properties, in terms of grain size, preferential orientation, and unit cell volume, in comparison to the ones of the material grown with no constraints, as we have found out by X-ray diffraction analyses. We have studied the effect of the PSC configuration on photoinduced absorption and time-resolved photoluminescence, complementary techniques that allow studying charge photogeneration and recombination. We have estimated electron diffusion length in the considered configurations observing a decrease when the material is confined in the MS scaffold with respect to a planar architecture. However, the presence of perovskite overlayer allows an overall recovering of long diffusion lengths explaining the record PV performances obtained with a device configuration bearing both the mesostructure and a perovskite overlayer. Our results suggest that performance in devices with perovskite overlayer is mainly ruled by the overlayer, whereas the mesoporous layer influences the contact properties.

Perovskite solar cells (PSCs) are awaking a great interest in the last 2–3 years due to the outstanding results in terms of photoconversion efficiency from low-cost deposition techniques.¹ In this period reported efficiencies in all-solid devices has moved from 10 to 11%^{2,3} to certified 20.1% (http://www.nrel.gov/ncpv/images/efficiency_chart.jpg). This spectacular evolution, with no precedent in any other photovoltaic technology, has been obtained mainly by an optimization of the PSC preparation processes. However, despite these progresses many aspects of PSCs working principles remain not completely understood. Thus, a deeper knowledge of the

physical processes occurring in such devices will undoubtedly help to further improves their performances.

In this frame, one of the most intriguing aspects that first surprised researchers, involved in this emerging technology, was the retrieved obtainment of outstanding photovoltaic (PV) performances notwithstanding important device configuration variations. In one of the first reports, Kim et al. produced a

Received: March 7, 2015

Accepted: April 8, 2015

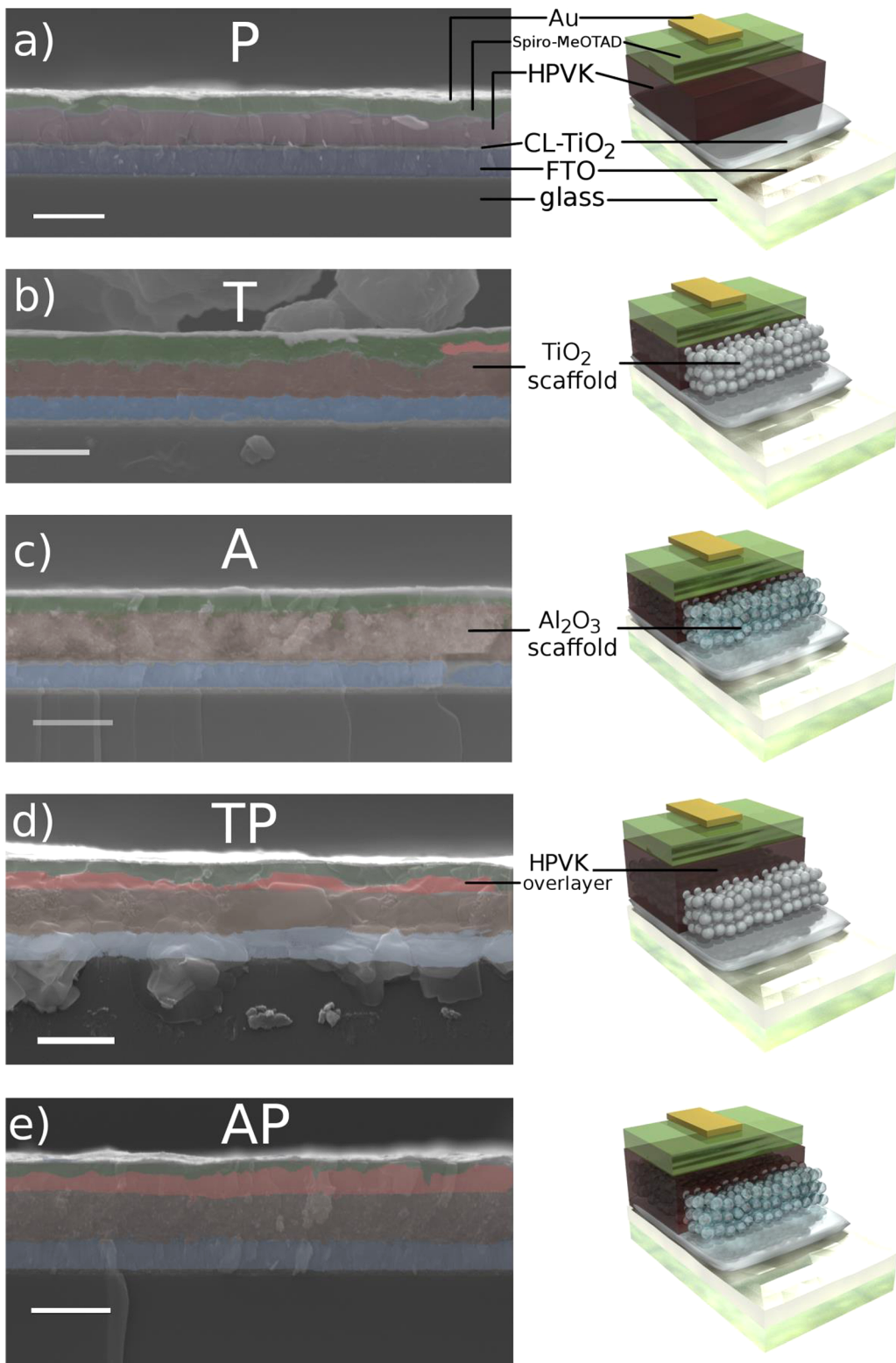


Figure 1. Cross-sectional scanning electron micrographs (SEM) of the devices studied (left) and schematic view (right); (a) P, (b) T, (c) A, (d) TP and (e) AP devices. Images were obtained using as the background the image of the secondary electron ray mode view that is most rich in texture surface details overlapped with a color coded semitransparent retrodispersed electrons image to identify unambiguously the thickness of embedded perovskite inside scaffold and the overlaid perovskite. Scale bar is a 1 μm . Color code: Au (white), Spiro-MeOTAD (green), HPVK overlayer (dark pink) embedded HPVK (gray-red), FTO (blue-gray). Supporting Information Figure S3 and S4 are the corresponding raw SEM images as obtained without color composite post-treatment.

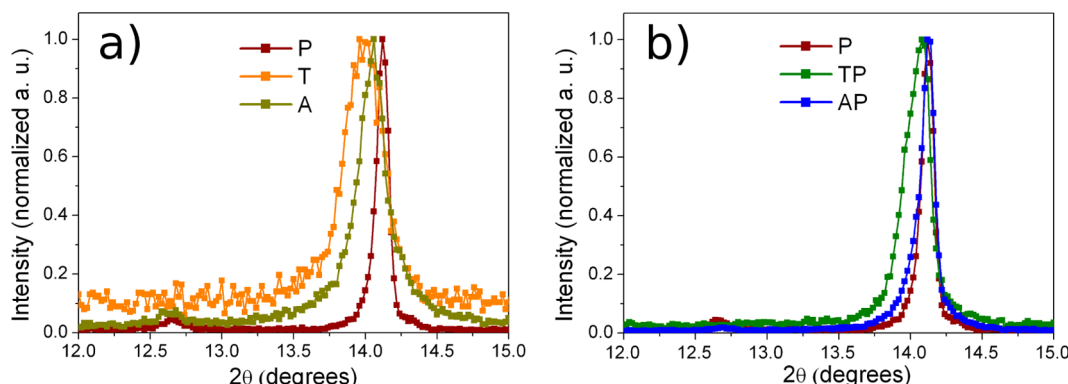
PSC with a configuration mimicking dye sensitized configuration with a TiO₂ scaffold, supposedly acting as electron transport material (ETM), where $\text{CH}_3\text{NH}_3\text{PbI}_3$ hybrid halide

perovskite (HPVK) was fully infiltrated.⁴ Practically at the same time, Lee et al. reported also excellent efficiencies using an infiltrated insulating scaffold of Al₂O₃, that cannot act as ETM.²

Table 1. Mass and Geometrical Characteristics of HPVK Samples Calculated Experimentally by SEM, Pore Size Determination, and XRD Analysis^a

device	mesoporous scaffold thickness	porosity ^b	overlayer thickness	overlayer surface coverage ^c	perovskite mass weight/active area ^d	crystallite size ^e	<i>a</i> ^f	<i>c</i> ^f	unit cell volume	parameter March–Dollase ^g
	[nm]	[%]	[nm]	[%]	[g/cm ²]	[nm]	[Å]	[Å]	[Å ³]	
P			440 ± 40	65	12.0 ± 1.2 × 10 ⁻⁵	145 ± 10	8.868(1)	12.650(3)	994.4(2)	0.44(1)**
T	440 ± 60	28			5.2 ± 0.7 × 10 ⁻⁵	26 ± 2	8.896(1)	12.633(2)	1000(1)	0.38(2)*
A	640 ± 40	32			8.5 ± 0.1 × 10 ⁻⁵	25 ± 2	8.893(4)	12.647(5)	1000(1)	0.66(3)*
TP	540 ± 20	28	170 ± 70	66	11.0 ± 2.0 × 10 ⁻⁵	134 ± 12 ^h	8.871(1)	12.62(2)	994(1)	0.25(2)**
AP	620 ± 30	32	270 ± 50	28	11.3 ± 0.9 × 10 ⁻⁵	150 ± 12 ^h	8.875(1)	12.646(4)	996.2(4)	0.49(3)**

^aErrors on the last significant digit are shown in parentheses. ^bExperimental porosity from Ar isotherm at 77 K. ^cOverlayer surface coverage evaluated using the high contrast color threshold tool of ImageJ;¹⁰ see Supporting Information Figure S6. ^dCalculated total mass quantity of perovskite deposited accounted by embedded perovskite inside the mesoporous layer and perovskite overlayer per square centimeter of device. The crystal density of HPVK was obtained elsewhere.⁹ ^eDetermined by microstructure analysis implemented in FullProf from the XRD data. (^) indicates that crystallite size reported is for the overlayer. ^f*a* and *c* unit cell parameters of perovskite tetragonal structure. ^gCalculated ref 11. Preferential orientation along *(001) and **(110) directions. P = glass/TiO₂–CL/HPVK/spiro-MeOTAD/Au, T = glass/TiO₂–CL/HPVK infiltrated inside mesoporous TiO₂/spiro-MeOTAD/Au, A = glass/TiO₂–CL/HPVK infiltrated inside mesoporous Al₂O₃/spiro-MeOTAD/Au, TP = glass/TiO₂–CL/HPVK infiltrated inside mesoporous TiO₂/HPVK overlayer/spiro-MeOTAD/Au, and AP = glass/TiO₂–CL/HPVK infiltrated inside mesoporous Al₂O₃/HPVK overlayer/spiro-MeOTAD/Au.

**Figure 2.** Experimental XRD pattern of the plane (110) of the tetragonal HPVK for (a) P, T, and A type substrates and (b) P, TP, and AP substrates. P sample is included in both graphs to better comparing the broadening of the signal between samples.

Later, it was shown that samples presenting a HPVK overlayer on top of the nanostructured scaffold both using alumina⁵ or titania⁶ possessed higher PV performance. Moreover, planar devices demonstrated also a very high efficiency.⁷ The presence of mesostructured scaffold obviously constrains the perovskite crystal size to the nanostructure pore size, whereas planar samples presents a relative big grain size.⁷ This fact has implications in different material properties such as light absorption.⁸ However, a straight relationship with optical and transport properties and the device configuration has not been found yet. In this work, we have prepared HPVK layers with different configuration characterizing them by X-ray diffraction (XRD), photoinduced absorption (cw-PIA), and time-resolved photoluminescence (TRPL) in order to study the effect of configuration in the properties of layers and devices.

Several types of HPVK based devices were assembled. The set of devices studied comprises two groups: (1) complete working photovoltaic solar cell devices with planar configuration or containing either alumina or titania as metal oxide mesostructured scaffold, (Figure 1 and Supporting Information Figure S1) using compact TiO₂ and spiro-OMeTAD as selective electron and hole layers, respectively, and (2) probe devices assembled without compact TiO₂ or FTO layer and using inert PMMA layer instead of spiro-MeOTAD aiming at isolate particular photoinduced processes. Supporting Informa-

tion Figure S2 depicts schematically the devices prepared for this study together with the naming convention used for the devices. The sample nomenclature used hereafter to denote the different configuration is: P for planar HPVK, T for fully infiltrated sample with TiO₂ scaffold, A for fully infiltrated sample with Al₂O₃ scaffold, TP for samples with TiO₂ scaffold and HPVK overlayer, and AP for samples with Al₂O₃ scaffold and HPVK overlayer (see Figure 1).

As we want to study the effect of different device configurations, we have to rule out other effects such as the amount of deposited perovskite. We have determined the deposited HPVK quantity in each configuration by measuring the layer thickness and the surface coverage via scanning electron microscopy (SEM) imaging, the optical light absorption spectra for every device, the textural image characterization of the mesoporous layer and the Ar adsorption–desorption isotherms (see section S2 and Figures S7 and S8 in the Supporting Information). Cross-sectional (Figure 1) and top-view (Supporting Information Figure S5 and S6) SEM micrographs of the studied devices are used to calculate thickness and total coverage of the HPVK overlayer, which are reported, for clarity, in Table 1.

Total amount of HPVK deposited in the different configurations is estimated in Table 1 using SEM and textural characterization. We assume pores are fully filled with HPVK

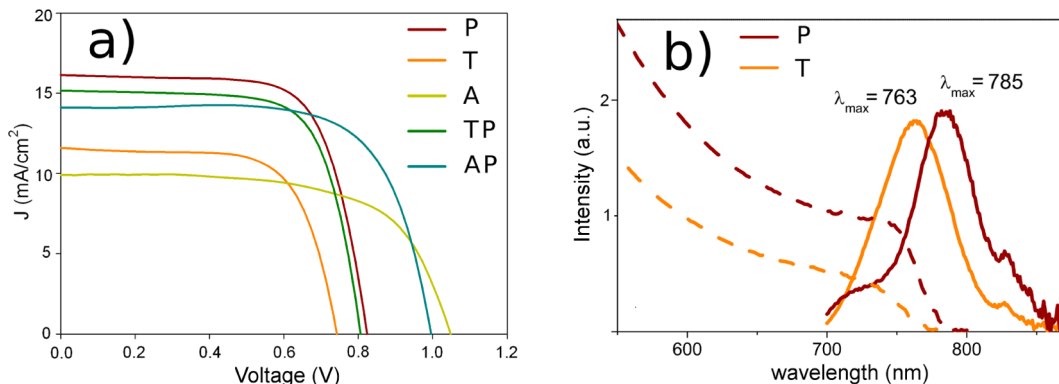


Figure 3. (a) Current–potential J – V curve of the studied devices under 1 sun illumination and voltage scan from open circuit to short circuit (see Supporting Information Figure S10 for forward voltage scan of the devices), (b) diffuse optical absorption (dashed line) and photoluminescence (solid line) spectra of the thin film device and the mesoporous cell without overlayer.

crystallites. The scaffold porosity has been measured experimentally by Ar desorption isotherm at 77 K, see Supporting Information Figure S7. The pore size distribution of alumina and titania mesoporous scaffolds is almost equal and it consists of a bimodal pore size centered at 4 and 22 nm width pore size, consequently HPVK grains of the same size can be inferred for infiltrated perovskite, see Supporting Information Figure S8. This point has been confirmed by XRD analysis, see below. The determined HPVK volume is converted to weight mass using the density for the bulk crystal material, 4.159 g/cm^3 .⁹ For simplicity, the same crystal density value is considered for infiltrated and overlayer HPVK. XRD indicates, however, that this assumption is not strictly true (see below) but the introduced error is estimated to be lower than those introduced by other geometrical factors and, consequently, is neglected. In addition the effective coverage of the overlayer, extracted from SEM images has been also taken into account (Supporting Information Figure S6), in order to calculate the perovskite mass weight. The profiles obtained clearly state that P, TP, or AP devices present similar amount of HPVK, whereas fully infiltrated samples, T and A, present a lower amount. In line with these estimations, the optical absorption of the devices at 635 nm (Supporting Information Figure S9) indicates similar differences in the amount of HPVK deposited depending of the device type.

The analysis of the XRD patterns for the different configurations provides very valuable information, indicating several differences between the perovskite growth as overlayer and the infiltrated perovskite growth inside the scaffold. The first difference is the smaller crystallite size of the T and A samples compared with P sample. T and A samples presented broader diffraction peaks, Figure 2a, corresponding to smaller grain size as it has been calculated by microstructure analysis, see Table 1. The crystallite size obtained from XRD is in good agreement with the pore size distribution of the scaffolds, see Supporting Information Figure S8. Samples TP and AP show an asymmetric diffraction peaks that can be deconvoluted by the presence of two grain sizes one corresponding to the infiltrated perovskite and another one corresponding to the HPVK overlayer with grain size similar than P sample, see Figure 2b and Supporting Information Figure S14. In addition to these expected results, it is worth noticing the additional changes detected in the structural properties of HPVK depending on whether it grows infiltrated in the mesostructure or not. Our study reveals that the preferred orientation axis

changes from (110) for the overlayer to (001) for infiltrated HPVK. This change is more important for the Al_2O_3 scaffold that shows higher preferential orientation. Preferential orientation has been quantified by the March–Dollase parameter,¹¹ see Table 1. When this dimensionless parameter presents a value equal to 1 sample presents random orientation, but when lower value than 1 is calculated preferential orientation is detected. The degree of preferential orientation is higher as the parameter separates from 1 value. Moreover, there is a clear enlargement of the crystal unit cell volume for the pore confined HPVK, see the shift in the diffraction peaks of A and T samples with respect to the P sample, Figure 2a, and unit cell parameters and unit cell volume in Table 1. XRD analyses indicate that the structural properties of perovskite (size, preferential orientation, and unit cell volume) are influenced by pore size but also by the nature of mesoporous scaffold. Note also that the use of PbCl_2 precursor instead of PbI_2 for HPVK synthesis can also affect the HPVK growth process inside the mesopores, as it has been recently pointed out.^{12–14} Our results are also in line with Choi et al., whom observed a difference between bulk perovskite and HPVK grown on mesostructured substrate.¹⁵ The collection of such observations implies that mesoporous layer (with infiltrated HPVK) and overlayer constitute in fact two layers with significantly different nature.

PSC devices have been fabricated reproducing the different configurations analyzed. We did not optimized the different architectures to obtaining record PV performances, instead we hold the material preparation procedures for the sake of the valuable comparison of the related material properties. J – V profiles and parameters obtained for the assembled working devices are shown in Figure 3a and Table 2, respectively. Also here, a clear trend is observed relating the quantity of deposited HPVK with the density of photocurrent, J_{sc} , extracted from the different devices. Higher content of HPVK implies higher J_{sc} . Furthermore, samples with alumina scaffold show higher open circuit voltage, V_{oc} , than samples with TiO_2 scaffold or without scaffold, as it has been previously observed,^{2,16} due to a lower recombination rate, which we have demonstrated by impedance spectroscopy.¹⁶ The physical origin of such observation could probably be related to the different structural properties such as the enhanced preferential orientation induced by alumina scaffold, discussed above. From such results, it can be extrapolated that V_{oc} is highly dependent on device architecture but J_{sc} is mainly dependent on the amount of HPVK deposited

Table 2. Best Performing Solar Cell Parameters under 1 Sun Illumination: Short Circuit Current, J_{sc} , Open Circuit Potential, V_{oc} , Fill Factor, FF, and Photoconversion Efficiency, η , As Obtained from Figure 3a^a

device	J_{sc} [mA/cm ²]	V_{oc} [mV]	FF [%]	η [%]
P	16.14	824	70.20	9.33
T	11.60	742	68.12	5.86
A	9.92	1048	63.86	6.64
TP	15.15	806	70.96	8.67
AP	14.11	996	69.58	9.78

^aSee Supporting Information Table S1.a for parameters obtained at forward and reverse voltage scan and Supporting Information Table S1.b for the average parameters for a batch of 10 solar cells. Supporting Information Figure S10.b shows the IPCE spectra with integrated photocurrent for the devices, in good agreement with photocurrent measurements from $J-V$ curves.

by a certain preparation method. However, it is worth noting that differences in deposition and crystal growth method can induce variations of the obtained J_{sc} .

With the aim rationalizing how and to what extent the mesostructuring of the substrate and the sample architecture would lead to differences in perovskite-based solar cells, here, we compare the photophysical processes occurring in the five perovskite active layers presented above. We first investigate PL from the HPVK active material embedded in working devices and in reference systems designed to isolate specific phenomena. For this analysis, HPVK was directly deposited on glass substrate. Sample P presents a PL band centered at 785 nm. This emission shifts to higher energy ($\lambda_{max} = 763$ nm) when the perovskite is fully infiltrated within an oxide mesoporous matrix (samples T and A), followed by a concordant shift of the absorption onset as shown in Figure 3b (and Supporting Information Figure S9). As the perovskite is deposited in every investigated system with the same procedure, specific differences induced by the oxide matrix should be taken into account to explain the observation. The constraint induced by the pores volume leads to the formation of smaller crystal in mesoporous layer compared to thin film architectures. The band edge shift related to the perovskite crystallite dimension has been recently demonstrated by growing large crystal via solution methods.^{17,18} Accordingly, the increase of the grains dimensions in planar configuration could be considered the main reasons of the absorption onset and emission maximum shifts. In general this behavior would promote an improvement of the charge collection in the NIR

region of the spectra for perovskite film containing large crystallites.

To further prove the effect of cell configuration on the perovskite photophysical properties, we employ quasi-steady-state photoinduced absorption (cw-PIA) spectroscopy. Figure 4a compares the in phase component of the photoinduced absorption spectra obtained from P/PMMA, TP/PMMA, and AP/PMMA. The only noticeable feature observed from cw-PIA spectra (Figure 4a) is a dominant contribution originating from the perovskite absorption ground-state bleaching around 760 nm. Depending on the samples, we noticed a slight shift that reflects the already mentioned different distribution of the grain dimension. It is very important to highlight that no significant differences are observed between the three spectra. A noteworthy electron injection from HPVK would induce a photoinduced absorption band in the region above 800 nm were TiO_2 electrons would absorb. We have previously observed that photoinjection of electrons from perovskite into TiO_2 scaffold was significantly lower than in other devices as a dye-sensitized cell.¹⁹ For the samples analyzed in this work, the effect is more marked, as no difference can be appreciated in IR region of the cw-PIA spectra between TP sample and P and AT samples (see Figure 4a). Consequently, we can reasonably exclude here an efficient electron transfer from perovskite to the mesoporous TiO_2 scaffold, as previously demonstrated. Very recently the value of PSCs capacitance was reported to be about 10 times less than would be expected for a solid-state dye sensitized cell using a similar NS TiO_2 film thickness,²⁰ suggesting that only the TiO_2 electron states near the FTO could be filled in such devices. This result nicely supports our observations. It is important to notice, however, that in the systems whose spectra is reported in Figure 4a, the absence of a hole accepting layer could also impact on the tendency of perovskite to inject electrons into the NS TiO_2 scaffold.

The main spectral features of the PIA spectra have been resolved via ultrafast transient absorption spectroscopy,²¹ decoupling the contribution from local electric fields.¹⁴ The ground-state bleaching recovering have been nicely correlated to the population of excitons/free charges, mostly recombining via radiative pathways. The strong dominant bleaching signal in the spectra of Figure 4a clearly indicates the massive contribution arising from free carriers accumulating within the perovskite films, despite the different substrate architecture monitored.⁴ In Figure 4b, the PIA spectra of the fully working devices are reported; in this case, a clear trend is observed for the TiO_2 -based devices. The bleaching signal decrease from P to TP to T. Interestingly, the photocurrent extracted from such

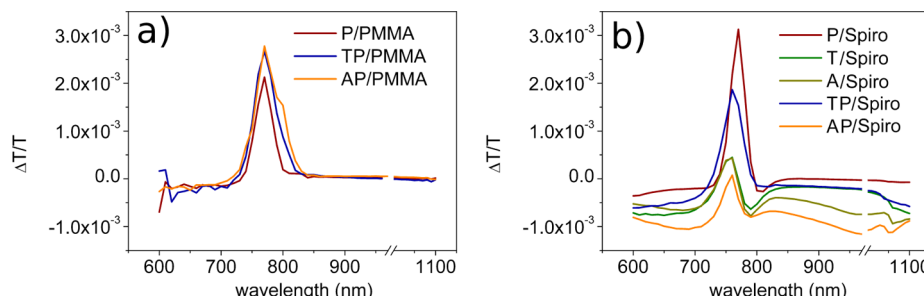


Figure 4. (a) cw-PIA spectra of P/PMMA, TP/PMMA, and AP/PMMA excited at 488 nm. (b) cw-PIA spectra for the set of working devices excited at 488 nm.

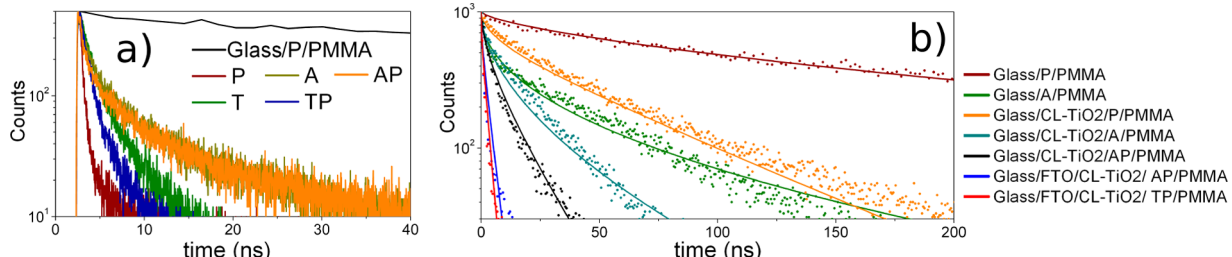


Figure 5. (a) PL decays of working devices and completely isolated glass/P/PMMA device. (b) PL decays with electron quenching layer and completely isolated glass/P/PMMA and glass/A/PMMA devices. PL decays recorded at 770 nm while exciting at 635 nm and collecting from the substrate side.

devices follows the same trend. As further discussed below, the reduction of the feature in TP compared to P would be justified by the increase of the radiative deactivations paths induced by the pores confinement of HPVK, which decreases the carrier lifetime. The reduction of the bleaching is also related to the amount of perovskite present in the investigated sample. As reported in Table 1, the samples without overlayer have less deposited perovskite, and thus, the decrease in the photo-induced absorption between TP and T should be related to the reduced carriers density caused by the decrease of the sample absorption. These findings points to that cw-PIA features intensity account for the different amount of charge stored by the different stacks with different crystal size of perovskite and very interestingly this correlates with the device photocurrent. Nevertheless, this hypothesis needs further research in order to be unambiguously confirmed.

In Al₂O₃-based devices the ground-state bleaching is still intense, but it is evidently pushed down by the negative absorption of Spiro-OMeTAD⁺ with the two well recognizable features at 710 and 980 nm.^{22,23} This fact suggests that in the continuous excitation regime, Spiro-OMeTAD extracts the holes more efficiently in Al₂O₃ than in TiO₂-based devices. The observation is not easy to rationalize, and frequency dependence cw-PIA analyses are being carried out to shine light on this aspect. At this stage, we could speculate that the behavior could be caused by the interface between Spiro-OMeTAD and the corresponding oxide material. In fact, even in the case of samples with overlayer, this does not cover completely the MS matrix allowing contacts between the scaffold and the hole selective contact, this in case of TiO₂-based device could lead to detrimental charge recombination processes even if the charge injected in the TiO₂ is proven to be poor. The different oxides also affect the perovskite active material, as we have shown with XRD analysis, via influencing the material growth and/or its defects nature and distribution, leading to different charge distribution in the two analyzed cases. These interesting observations could be, among others, to the ground of the usually observed higher V_{oc} obtainable in Al₂O₃ mesostructured perovskite solar cell.^{2,16}

Time-resolved PL decay is also a useful tool to probe the effect of configuration on perovskite devices. PL decays of complete PSCs are reported in Figure 5a. Sample excitation and PL detection are produced through substrate side (FTO). The decays are taken at the maximum of the PL band. All the samples show a strong PL quenching if compared to the isolated perovskite device glass/P/PMMA. Among the investigated samples, the P device shows the strongest quenching followed by mesostructured devices TP, T, AP, and A. PL quenching of the perovskite when coupled to active

materials (TiO₂) have been associated with charge extraction.^{24–26} However, as we have already discussed in previous works,¹⁹ porous media has influence on the radiative deactivation mechanism in perovskite materials, and extra deactivation processes altering the excited states decay should be considered in addition to the charge extraction for the different architectures.

Relevant perovskite layer parameters as electron diffusion coefficient, D , and electron diffusion length, L_d , can be obtained from the measurement of PL decay with and without electron extracting layer (in our case TiO₂) as it has been previously reported^{24,26} (see Table 3). Finite-difference time-domain

Table 3. Profiles for Electron D and L_d Obtained Using the Simple One Layer PL Decay 1-D Diffusion Model,²⁴ Exciting and Collecting from the Substrate Side

device	D (cm ² /s)	L_d (nm)
glass/CL-TiO ₂ /P/PMMA	0.010 ± 0.002	400 ± 30
glass/CL-TiO ₂ /A/PMMA	0.004 ± 0.001	60 ± 5
glass/CL-TiO ₂ /AP/PMMA	0.050 ± 0.010	260 ± 30
glass/FTO/CL-TiO ₂ /AP/PMMA	0.850 ± 0.100	1050 ± 90
glass/FTO/CL-TiO ₂ /TP/PMMA	0.780 ± 0.100	1000 ± 90

diffusion modeling of the PL decay in one-dimensional substrates were carried out to shed light on the charge collection efficiency of the devices by modeling the electron density, $n(x,t)$, in the HPVK layer according to same procedure reported elsewhere^{24,26} (see section S.5 in Supporting Information). It is important to highlight that the magnitudes obtained in this way has to be considered as estimation since several approximations are used for obtaining them. As a first approximation, we consider charge transfer at TiO₂ interface infinite, that is, electrons that attain the interface are immediately extracted, but this is not the case, as is pointed in ref 25. Moreover, according to this, only diffusion transport is considered, that is, there is no electrical field in the perovskite layer, and consequently, no drift transport is considered. It is no straightforward to evaluate the accurateness of this approach as there is no complete model of PSC performance but in a p-i-n scenario,²⁸ as many works point out, electrical fields^{29,30} could have an important effect in the transport. Finally, we consider for TP and AP case a simple effective layer and we do not take into account explicitly that is an infiltrated HPVK + HPVK overlayer. This last approximation is probably the origin of the discrepancies observed in the calculated D and L_d for samples with overlayer comparing illumination though the substrate with opposite side illumination (see Supporting Information Table S2). Note that this discrepancy does not exist for more uniform samples with no overlayer (P, T, and A), being a

reasonable verification of the model. For this reason, despite the roughness of the approach, we consider that valuable qualitative information can be obtained from this analysis.

Several interesting observations can be highlighted. Figure 5b compares the different PL decay behaviors. First, we compare isolated perovskite layers, with non-extracting contact: glass/P/PMMA and glass/A/PMMA with the corresponding layers including compact TiO_2 (CL-TiO_2) quencher, that is, glass/CL-TiO₂/P/PMMA and glass/CL-TiO₂/A/PMMA. Reduction of perovskite crystal size due to the constraints of alumina scaffold produces a significant decrease of both diffusion coefficient (0.010 and 0.004 cm²/s for P and A devices, respectively) and diffusion length (400 and 60 nm for P and A devices, respectively); see Table 3. As the model takes into account, the total amount of perovskite in both devices the reduction in L_d , which is more than 6-fold, has to be attributed mainly to the reduction of grain size. Surprisingly, glass/CL-TiO₂/AP/PMMA configuration presents a significantly lower reduction of L_d (260 nm) being of the same order than P sample. This fact is in a certain way unexpected, as we could consider AP sample as a series connection of a totally infiltrated layer with a overstanding perovskite layer, with transport restricted by the layer with the worst transport, but the observed behavior is opposite.

Perovskite overlayer is therefore a smart strategy to enhance solar cell performance as it increases the diffusion length to the same range of the planar cells.³¹ This fact suggests that perovskite infiltrated in nanostructured layer plays a minor role on cell performance in comparison with the perovskite overlayer. In this sense, the main role of nanostructure scaffold is to help in the perovskite growth process and modify the electron selective contact. In addition, the scaffold could promote an effect regarding electrical field distribution.²⁹ This conclusion is in good agreement with previous results. It has been observed a clearly differentiate behavior of nanostructured layer with infiltrated HPVK and perovskite overlayer by Kelvin force microscopy.²⁹ Besides, hysteresis detected in most of the PSC is strongly dependent on the contact nature,³² and it can be strongly reduced by adding a nanostructured TiO_2 film to the planar PSC configuration, observing and optimizing behavior for 200 nm thick TiO_2 nanostructured scaffold.³³

Different reasons could be at the source of this shortening of the PL decays that are attributable only to the contribution coming from the perovskite grown within the oxide. One hypothesis could be higher carrier densities for small grains leading to the radiative recombination increase. Related to this, in a recent study, PL decays components have been resolved in perovskite film, employing two-photon fluorescence microscopy, and evident inhomogeneitys have been found in the film, in particular, different carrier concentrations and, thus, different PL lifetimes were found at grain boundaries and at imperfect interfaces between perovskite and surrounding layers.³⁴ Accordingly, a different perovskite defect/trap filling within the pores induced by the oxide surface contact could also contribute to the PL decay shortening. Recently Leijtens et al.³⁵ reported a comparison between thin film and mesostructured perovskite solar cells. Through photoelectron spectroscopy they found evidence of a large distribution of sub-band-gap states (traps for electrons: Pb^{1+} and Pb^{2+}), whose distribution is influenced by the presence of a scaffold. Moreover, they found that mesoporous scaffold rises the Fermi levels of perovskite due to surface defects (under-coordinate halides acting as shallow donors) or to electrostatic interactions. Compared to

the P configuration, this energetic landscape takes to lower PL quantum efficiency and transport. In fact, the reduction of the PL decay lifetime that we attribute to the perovskite confinement in the oxide matrix is an indication of a reduced carries diffusion length within this material phase.

The comparison of our results ($\approx 0.010 \text{ cm}^2/\text{s}$ and $\approx 400 \text{ nm}$ for D and L_d , respectively) with the previous ones reported using the same HPVK growth method, with P configuration and PCBM as electron quenching layer²⁴ ($0.042 \text{ cm}^2/\text{s}$ and 1069 nm for D and L_d , respectively) points to an effect of the selective contact in the effective diffusion coefficient and diffusion length. This effect should arise probably from the effect of surface recombination as a reduced charge extraction also enhances surface recombination. To this extent, D and L_d profiles are affected also by the type of electron quenching layer, CL-TiO₂ instead of PCBM-based layer in this case. Another interesting trend observed in the PL decays, is that the FTO is playing a role in the electron quenching process. We have prepared AP devices using as ETM the combination glass/FTO/CL-TiO₂ or glass/CL-TiO₂ (see Figure 5b, Table 3, and Supporting Information Figure S13a). Both D and L_d are boosted to $\sim 1 \mu\text{m}$ when FTO is underlaying the CL-TiO₂. We hypothesize that it is due to the FTO improving the electron conduction over the electron quenching layer avoiding charge accumulation in selective parts of TiO_2 and, therefore, improving the charge extraction. Finally, similar L_d has been detected for TP and AP (see Figure 5b and Supporting Information Figure S13b), pointing to very similar working principles, in good agreement with cw-PIA measurements.

In summary, we have analyzed different PSCs device configurations, spanning from planar, P, to mesostructured ones, bearing fully infiltrated titania, T, or alumina, A, scaffolds and with perovskite overlayer on top of the nanostructured layer, respectively, TP and AP. We have analyzed and compared those samples by XRD, cw-PIA, and time-resolved luminescence measurements. XRD analysis indicates that structural properties (grain size, preferential orientation, and unit cell volume) of infiltrated HPVK are different than those of perovskite grown with no constraints. In addition, the nature of mesoporous scaffold affects the final structural properties and high degree of preferential orientation has been detected for alumina scaffold. The strong dominant bleaching signal in the cw-PIA spectra clearly indicates the massive contribution arising from free carriers accumulating within the perovskite film despite the different substrate architecture monitored. Furthermore, the reduction of the bleaching is also related to the amount of perovskite present in the investigated sample. Moreover, no significant injection from HPVK into titania scaffold was detected pointing to a similar working principles than alumina samples. From PL decay, qualitative values of diffusion coefficient and diffusion length have been obtained. A reduction of L_d with the perovskite grain size has detected by comparing P and A samples. Nevertheless, when a perovskite overlayer is grown on top of the nanostructured scaffold, large L_d is recovered. Our results indicate that infiltrated mesoporous layer and overlayer have a significant different nature and play a different role. The HPVK overlayer is the main responsible of cell performance while the nanostructured plays an important role modifying the properties of the electron selective contact. Consequently, large L_d have been obtained for AP and TP samples as in the case of P samples, sensibly higher that the observed in totally infiltrated samples as A. The nature of electron-selective contact also affects the diffusion coefficient

diffusion length of the devices, likely by its effect in charge transfer and interfacial recombination. We consider that these results will help in the interpretation of PSC and how cell configuration affects cell performance. Undoubtedly a complete understanding of PSC working principles will further move the performances already obtained.

Methods

Devices Preparation. All the studied substrates were prepared over FTO (Pilkington TEC15, $15\ \Omega/\text{sq}$ resistance), which were previously etched with zinc powder and HCl (2 M) to obtain $0.224\ \text{cm}^2$ of active electrode area per pixel. The FTOs substrates were cleaned with soap (Hellmanex), deionized water, acetone, ethanol, and isopropanol inside an ultrasonic generator during 10 min for every solvent. Before the deposition of electron selective contacts, substrates were treated in a UV–O₃ chamber for 30 min. A 50 nm thick TiO₂ compact layer was deposited by spin-coating (2000 rpm, 60 s) with a mildly acidic solution of titanium isopropoxide in ethanol and then was heated at 500 °C for 30 min.³⁶ The ~500 nm mesoporous TiO₂ layer was deposited by spin coating at 2000 rpm during 60 s using a TiO₂ paste (Dyesol 18NRT, 20 nm average particle size) diluted in terpineol (1:3, weight ratio). After drying at 80 °C, the TiO₂ layers were heated to 470 °C at this temperature for 30 min and cooled to room temperature. The ~500 nm mesoporous Al₂O₃ scaffold was deposited by spin-coating at 2000 rpm during 60 s a colloidal dispersion of <50 nm Al₂O₃ nanoparticles (Sigma-Aldrich, product number 702129 diluted 2:1 (v/v) of commercial dispersion/isopropanol) followed by drying at 150 °C for 1 h. Thin-film devices of MAPbI_{3-x}Cl_x perovskite were deposited by spin coating 100 μL of perovskite precursor, 40% (w/w) DMF solution of CH₃NH₃I and PbCl₂ (3:1 molar ratio), onto flat TiO₂ substrates at 2000 rpm for 60 s. Then, the films were placed on a heated furnace at 100 °C under air stream. Devices with an overlayer of perovskite were prepared using the same before solution onto mesostructured scaffolds and the devices without such overlayer were prepared using a more diluted perovskite precursor in solution (30% w/w instead of 40%). Working devices based on perovskite-adsorbed films were covered with a HTM layer by spin coating at 4000 rpm for 60 s outside of the glovebox. The HTM recipe was prepared dissolving 72.3 mg of (2,2',7,7'-tetrakis(*N,N*-di-*p*-methoxyphenylamine)-9,9-spirobifluorene) (spiro-MeOTAD), 28.8 μL of 4-*tert*-butylpyridine, and 17.5 μL of a stock solution of 520 mg/mL lithium bis(trifluoromethylsulfonyl)imide in acetonitrile in 1 mL of chlorobenzene. Finally, 60 nm of gold was thermally evaporated in the vacuum chamber on top of the device to form the electrode contacts. Devices with a top-layer of PMMA were fabricated in the same way as before, but instead of the HTM layer, a 30 mg/mL solution in chloroform of PMMA (Sigma-Aldrich, product number 182230) was spin-coated at 2000 rpm during 60 s directly onto the perovskite substrate.

Devices Characterization. Current–voltage curves were recorded under AM 1.5 100 mW cm⁻² simulated sunlight (ABET Technologies Sun 2000) with a Keithley 2400, previously calibrated with an NREL-calibrated Si solar cell. The measurements were performed using a 0.1 cm² mask. The incident monochromatic photon-to-current conversion (IPCE) spectra were performed using a 150 W Xe lamp coupled with a computer controlled monochromator being the photocurrent measured by an optical power meter 70310 from Oriel Instruments and using a Si photodiode to calibrate the system. Impedance spectroscopy measurements were carried out by

means of a Nova equipped PGSTAT-30 from Autolab under 1 sun light illumination conditions at different forward voltage bias and applying a 20 mV voltage perturbation over the constant applied bias with the frequency ranging between 1 MHz and 0.01 Hz. Impedance measurements at different V_{oc} were carried out using different neutral filters on the top of the device. SEM micrographs of the samples were carried out using a JSM-7000F JEOL 216 FEG-SEM system using secondary and retrodispersed electron beams. The textural properties characterization of the mesoporous scaffolds (TiO₂ and Al₂O₃) were evaluated from Ar adsorption–desorption isotherms at -196 °C using a Micromeritics ASAP 2020. The studied samples were prepared using the same colloidal dispersion and heating process used for the spin-coated mesosuperstructured scaffolds in the devices. Pore size distribution (PSD), average mesopore size, and pore volume were determined and the BET equation was used to calculate the surface area. Porosity is calculated using 3.90 and 3.97 g/cm³ as the real density values for TiO₂ and Al₂O₃ particles, respectively. PSD and cumulative pore volume were obtained by NL-DFT methods using sphere/cylinder shape pore model as implemented in Novawin2 by Quantachrome. X-ray diffraction patterns were collected on a Siemens DS000 diffractometer using copper K α radiation, in $\theta/2\theta$ geometry from P, T, A, TP, and AP substrates assembled without spiro-MeOTAD or gold layer. Rietveld refinements were performed using FullProf suite of programs.³⁷ In all cases, a multiphase fitting was performed (FTO, plus HPVK phases were considered). Samples in which only the Al₂O₃ scaffold was grown (without perovskite phase) showed no diffraction peaks. In the case of TiO₂ only a small peak corresponding to anatase was detected. Peak shape was described using a pseudo-Voigt function, and crystalline size has been determined by implemented in FullProf. The contribution from the instrument was determined by measuring LaB₆ standard in the same conditions. Preferred orientation was treated by means of March–Dollase correction.¹¹

Photophysical Characterization. Cw-PIA spectra were recorded using a white probe light generated by a 250 W tungsten-halogen lamp that was superimposed to a square-wave modulated laser (spectra physics, 50 mW nominal power, $\lambda = 488\ \text{nm}$) as excitation. The white probe light passed through a first monochromator (Princeton Acton Spectra Pro) before being focused on the sample in a spot of 0.5 cm². The light transmitted through the sample was focused onto a second monochromator and detected by a silicon photodiode connected to a current amplifier (femto DLPICA200) and then to a lock-in amplifier (Stanford Research System model SR 830). Intensity of approximately 12 mW cm⁻² and modulation frequency of 170 Hz was used for the laser excitation. Time resolved and steady state photoluminescence measurements were performed using time correlated single photon counting (TCSPC) apparatus of Hamamatsu FL980, 50 ps time resolution with deconvolution analysis. Pulsed excitation source at 635 nm, with a typical average power at 20 MHz of 0.13 mW, was employed to excite the samples.

ASSOCIATED CONTENT

Supporting Information

Devices preparation protocol, SEM pictures, textural characterization of the mesoporous samples by argon adsorption–desorption isotherms, light absorption and PL, *J–V* characterization, model for determination of electron diffusion

coefficients and diffusion lengths, dependence of the exciting/collecting side in the PL decays, and XRD study of the devices. This material is available free of charge via the Internet at <http://pubs.acs.org>.

■ AUTHOR INFORMATION

Corresponding Authors

*E-mail: Andrea.Listorti@iit.it.

*E-mail: sero@uji.es.

Author Contributions

○(A.L., E.J.J.-P.) These authors contributed equally to this work.

Notes

The authors declare no competing financial interest.

■ ACKNOWLEDGMENTS

This work was supported by the Universitat Jaume I (project 12I361.01/1), by Spanish MINECO (MAT2013-47192-C3-1-R), by EFOR (Iniziativa CNR per il Mezzogiorno L. 191/2009 art. 2 comma 44), by PON-MAAT (Project Number: PON02_00563_3316357-CUP B31C12001230005), by PON-FORM@BEYOND-NANO, and by Regione PUGLIA (APQ Reti di Laboratorio, project "PHOEBUS" cod. 31). The authors gratefully acknowledge Dr. Paolo Perazzelli for fruitful discussion.

■ REFERENCES

- (1) Jeon, N. J.; Noh, J. H.; Yang, W. S.; Kim, Y. C.; Ryu, S.; Seo, J.; Seok, S. I. Compositional Engineering of Perovskite Materials for High-Performance Solar Cells. *Nature* **2015**, *517*, 476–480.
- (2) Lee, M. M.; Teuscher, J.; Miyasaka, T.; Murakami, T. N.; Snaith, H. J. Efficient Hybrid Solar Cells Based on Meso-Superstructured Organometal Halide Perovskites. *Science* **2012**, *338*, 643–647.
- (3) Kim, H.-S.; Lee, C.-R.; Im, J.-H.; Lee, K.-B.; Moehl, T.; Marchioro, A.; Moon, S.-J.; Humphry-Baker, R.; Yum, J.-H.; Moser, J. E.; et al. Lead Iodide Perovskite Sensitized All-Solid-State Submicron Thin Film Mesoscopic Solar Cell with Efficiency Exceeding 9%. *Sci. Rep.* **2012**, *2*, 591.
- (4) Kim, H.-S.; Mora-Sero, I.; Gonzalez-Pedro, V.; Fabregat-Santiago, F.; Juarez-Perez, E. J.; Park, N.-G.; Bisquert, J. Mechanism of Carrier Accumulation in Perovskite Thin-Absorber Solar Cells. *Nat. Commun.* **2013**, *4*, 2242.
- (5) Ball, J. M.; Lee, M. M.; Hey, A.; Snaith, H. J. Low-Temperature Processed Meso-Superstructured to Thin-Film Perovskite Solar Cells. *Energy Environ. Sci.* **2013**, *6*, 1739–1743.
- (6) Heo, J. H.; Im, S. H.; Noh, J. H.; Mandal, T. N.; Lim, C.-S.; Chang, J. A.; Lee, Y. H.; Kim, H.-j.; Sarkar, A.; Nazeeruddin, M. K.; et al. Efficient Inorganic–Organic Hybrid Heterojunction Solar Cells Containing Perovskite Compound and Polymeric Hole Conductors. *Nat. Photonics* **2013**, *7*, 486–491.
- (7) Liu, M.; Johnston, M. B.; Snaith, H. J. Efficient Planar Heterojunction Perovskite Solar Cells by Vapour Deposition. *Nature* **2013**, *501*, 395–398.
- (8) D’Innocenzo, V.; Grancini, G.; Alcocer, M. J. P.; Kandada, A. R. S.; Stranks, S. D.; Lee, M. M.; Lanzani, G.; Snaith, H. J.; Petrozza, A. Excitons versus Free Charges in Organo-Lead Tri-Halide Perovskites. *Nat. Commun.* **2014**, *5*, 3586.
- (9) Stoumpos, C. C.; Malliakas, C. D.; Kanatzidis, M. G. Semiconducting Tin and Lead Iodide Perovskites with Organic Cations: Phase Transitions, High Mobilities, and Near-Infrared Photoluminescent Properties. *Inorg. Chem.* **2013**, *52*, 9019–9038.
- (10) Schneider, C. A.; Rasband, W. S.; Eliceiri, K. W. NIH Image and to ImageJ: 25 Years of Image Analysis. *Nat. Methods* **2012**, *9*, 671–675.
- (11) Dollase, W. Correction of Intensities for Preferred Orientation in Powder Diffractometry: Application of the March Model. *J. Appl. Crystallogr.* **1986**, *19*, 267–272.
- (12) Colella, S.; Mosconi, E.; Pellegrino, G.; Alberti, A.; Guerra, V. L. P.; Masi, S.; Listorti, A.; Rizzo, A.; Condorelli, G. G.; De Angelis, F.; et al. Elusive Presence of Chloride in Mixed Halide Perovskite Solar Cells. *J. Phys. Chem. Lett.* **2014**, *5*, 3532–3538.
- (13) Grancini, G.; Marras, S.; Prato, M.; Giannini, C.; Quart, C.; De Angelis, F.; De Bastiani, M.; Eperon, G. E.; Snaith, H. J.; Manna, L.; et al. The Impact of the Crystallization Processes on the Structural and Optical Properties of Hybrid Perovskite Films for Photovoltaics. *J. Phys. Chem. Lett.* **2014**, *5*, 3836–3842.
- (14) Roiati, V.; Mosconi, E.; Listorti, A.; Colella, S.; Gigli, G.; Angelis, F. D. Stark Effect in Perovskite/TiO₂ Solar Cells: Evidence of Local Interfacial Order. *Nano Lett.* **2014**, *14*, 2168–2174.
- (15) Choi, J. J.; Yang, X.; Norman, Z. M.; Billinge, S. J. L.; Owen, J. S. Structure of Methylammonium Lead Iodide within Mesoporous Titanium Dioxide: Active Material in High-Performance Perovskite Solar Cells. *Nano Lett.* **2014**, *14*, 127–133.
- (16) Suarez, B.; Gonzalez-Pedro, V.; Ripolles, T. S.; Sanchez, R. S.; Otero, L.; Mora-Sero, I. Recombination Study of Combined Halides (Cl, Br, I) Perovskite Solar Cells. *J. Phys. Chem. Lett.* **2014**, *5*, 1628–1635.
- (17) Dang, Y.; Liu, Y.; Sun, Y.; Yuan, D.; Liu, X.; Lu, W.; Liu, G.; Xia, H.; Tao, X. Bulk Crystal Growth of Hybrid Perovskite Material CH₃NH₃PbI₃. *CrystEngComm* **2015**, *17*, 665–670.
- (18) D’Innocenzo, V.; Srimath Kandada, A. R.; De Bastiani, M.; Gandini, M.; Petrozza, A. Tuning the Light Emission Properties by Band Gap Engineering in Hybrid Lead Halide Perovskite. *J. Am. Chem. Soc.* **2014**, *136*, 17730–17733.
- (19) Roiati, V.; Colella, S.; Lerario, G.; Marco, L. D.; Rizzo, A.; Listorti, A.; Gigli, G. Investigating Charge Dynamics in Halide Perovskite-Sensitized Mesostructured Solar Cells. *Energy Environ. Sci.* **2014**, *7*, 1889–1894.
- (20) O’Regan, B. C.; Barnes, P. R. F.; Li, X.; Law, C.; Palomares, E.; Marin-Beloqui, J. M. Opto-Electronic Studies of Methylammonium Lead Iodide Perovskite Solar Cells with Mesoporous TiO₂: Separation of Electronic and Chemical Charge Storage, Understanding Two Recombination Lifetimes, and the Evolution of Band Offsets during J–V Hysteresis. *J. Am. Chem. Soc.* **2015**, DOI: 10.1021/jacs.5b00761.
- (21) Deschler, F.; Price, M.; Pathak, S.; Klintberg, L.; Jarusch, D. D.; Higler, R.; Huettner, S.; Leijtens, T.; Stranks, S. D.; Snaith, H. J.; et al. High Photoluminescence Efficiency and Optically-Pumped Lasing in Solution-Processed Mixed Halide Perovskite Semiconductors. *J. Phys. Chem. Lett.* **2014**, *5*, 1421–1426.
- (22) Snaith, H. J.; Petrozza, A.; Ito, S.; Miura, H.; Grätzel, M. Charge Generation and Photovoltaic Operation of Solid-State Dye-Sensitized Solar Cells Incorporating a High Extinction Coefficient Indolene-Based Sensitizer. *Adv. Funct. Mater.* **2009**, *19*, 1810–1818.
- (23) Bi, D.; Yang, L.; Boschloo, G.; Hagfeldt, A.; Johansson, E. M. J. Effect Different Hole Transport Materials on Recombination in CH₃NH₃PbI₃ Perovskite-Sensitized Mesoscopic Solar Cells. *J. Phys. Chem. Lett.* **2013**, *4*, 1532–1536.
- (24) Stranks, S. D.; Eperon, G. E.; Grancini, G.; Menelaou, C.; Alcocer, M. J. P.; Leijtens, T.; Herz, L. M.; Petrozza, A.; Snaith, H. J. Electron–Hole Diffusion Lengths Exceeding 1 Micrometer in an Organometal Trihalide Perovskite Absorber. *Science* **2013**, *342*, 341–342.
- (25) Wojciechowski, K.; Stranks, S. D.; Abate, A.; Sadoughi, G.; Sadhanala, A.; Kopidakis, N.; Rumbles, G.; Li, C.-Z.; Friend, R. H.; Jen, A. K. Y.; et al. Heterojunction Modification for Highly Efficient Organic–Inorganic Perovskite Solar Cells. *ACS Nano* **2014**, *8*, 12701–12709.
- (26) Xing, G.; Mathews, N.; Sun, S.; Lim, S. S.; Lam, Y. M.; Grätzel, M.; Mhaisalkar, S.; Sum, T. C. Long-Range Balanced Electron- and Hole-Transport Lengths in Organic–Inorganic CH₃NH₃PbI₃. *Science* **2013**, *342*, 344–347.
- (27) Liang, P.-W.; Chueh, C.-C.; Xin, X.-K.; Zuo, F.; Williams, S. T.; Liao, C.-Y.; Jen, A. K.-Y. High-Performance Planar-Heterojunction

Solar Cells Based on Ternary Halide Large-Band-Gap Perovskites.

Adv. Energy Mater. **2014**, DOI: 10.1002/aenm.201400960.

(28) Edri, E.; Kirmayer, S.; Mukhopadhyay, S.; Gartsman, K.; Hodes, G.; Cahen, D. Elucidating the Charge Carrier Separation and Working Mechanism of $\text{CH}_3\text{NH}_3\text{PbI}_{3-x}\text{Cl}_x$ Perovskite Solar Cells. *Nat. Commun.* **2014**, *5*, 3461.

(29) Bergmann, V. W.; Weber, S. A. L.; Javier Ramos, F.; Nazeeruddin, M. K.; Grätzel, M.; Li, D.; Domanski, A. L.; Lieberwirth, I.; Ahmad, S.; Berger, R. Real-Space Observation of Unbalanced Charge Distribution Inside a Perovskite-Sensitized Solar Cell. *Nat. Commun.* **2014**, *5*.

(30) Guerrero, A.; Juarez-Perez, E. J.; Bisquert, J.; Mora-Sero, I.; Garcia-Belmonte, G. Electrical Field Profile and Doping in Planar Lead Halide Perovskite Solar Cells. *Appl. Phys. Lett.* **2014**, *105*, 133902.

(31) Gonzalez-Pedro, V.; Juarez-Perez, E. J.; Arsyad, W.-S.; Barea, E. M.; Fabregat-Santiago, F.; Mora-Sero, I.; Bisquert, J. General Working Principles of $\text{CH}_3\text{NH}_3\text{PbX}_3$ Perovskite Solar Cells. *Nano Lett.* **2014**, *14*, 888–893.

(32) Shao, Y.; Xiao, Z.; Bi, C.; Yuan, Y.; Huang, J. Origin and Elimination of Photocurrent Hysteresis by Fullerene Passivation in $\text{CH}_3\text{NH}_3\text{PbI}_3$ Planar Heterojunction Solar Cells. *Nat. Commun.* **2014**, *5*.

(33) Jeon, N. J.; Noh, J. H.; Kim, Y. C.; Yang, W. S.; Ryu, S.; Seok, S. I. Solvent Engineering for High-Performance Inorganic–Organic Hybrid Perovskite Solar Cells. *Nat. Mater.* **2014**, *13*, 897–903.

(34) Wen, X.; Sheng, R.; Ho-Baillie, A. W. Y.; Benda, A. v.; Woo, S.; Ma, Q.; Huang, S.; Green, M. A. Morphology and Carrier Extraction Study of Organic–Inorganic Metal Halide Perovskite by One- and Two-Photon Fluorescence Microscopy. *J. Phys. Chem. Lett.* **2014**, *5*, 3849–3853.

(35) Leijtens, T.; Stranks, S. D.; Eperon, G. E.; Lindblad, R.; Johansson, E. M. J.; McPherson, I. J.; Rensmo, H. a.; Ball, J. M.; Lee, M. M.; Snaith, H. J. Electronic Properties of Meso-Superstructured and Planar Organometal Halide Perovskite Films: Charge Trapping, Photodoping, and Carrier Mobility. *ACS Nano* **2014**, *8*, 7147–7155.

(36) Eperon, G. E.; Burlakov, V. M.; Docampo, P.; Goriely, A.; Snaith, H. J. Morphological Control for High Performance, Solution Processed Planar Heterojunction Perovskite Solar Cells. *Adv. Funct. Mater.* **2014**, *24*, 151–157.

(37) Rodriguez-Carvajal, J. FULLPROF: A Program for Rietveld Refinement and Pattern Matching Analysis. *Abstracts of the Satellite Meeting on Powder Diffraction of the XV Congress of the IUCr* **1990**, 127.